

Improved Kinematic Models for Two-Link Helical Micro/Nano-Swimmers

Ahmet Fatih Tabak, *Member, IEEE*, Serhat Yesilyurt, *Senior Member, IEEE*

Abstract— Accurate prediction of the three-dimensional trajectories of micro/nano-swimmers is a key element as to achieve high precision motion control in therapeutic applications. Rigid-body kinematics of such robotic systems is dominated by viscous forces. The induced flow field around a two-link swimmer is investigated with a validated computational fluid dynamics (CFD) model. Force-free-swimming constraints are employed in order to simulate motion of bacteria-like swimmers in viscous medium. The fluid resistance exerted on the body of the swimmer is quantified by an improved resistance matrix, which is embedded in a validated resistive force theory (RFT) model, based on complex-impedance approach. Parametric studies confirmed that the hydrodynamic interaction between body and tail are of great importance in predicting the trajectories for such systems.

Index Terms—Biological cells, Biomechanics, Fluidic microsystems, Hydrodynamics, Numerical models, Robot kinematics, Velocity measurement

I. INTRODUCTION

Swimming micro- and nano-robots in literature are presented as the candidates of minimal-invasive surgery tools to handle high precision therapeutic operations such as retina repair [1], [2]. Based on observations on bacteria and spermatozoa, and via some macro and micro-scale experiments, propulsion mechanisms of natural micro-swimmers are established as viable actuation means for motile autonomous swimming micro robots [3]-[10]. Propulsion mechanisms of bacteria and spermatozoa are based on wave propagation carried out by slender tail structures actuated by nano-scale motors [11]. The motivation of this work is to identify the role of hydrodynamic interactions between body and tail on the effective drag force and rigid-body kinematics of bacteria species, and to present modeling tools that improve the predictability of swimming trajectories of bacteria, which are to be incorporated in cybernetic micro/nano-robotic

This paper was submitted for review on 03.24.2013, conditionally accepted on 07.09.2013. Revised version was submitted for review on 08.05.2013, accepted as a regular paper for nanorobotics special issue on 08.22.2013.

A. F. Tabak was a Ph.D. candidate with the Department of Mechatronics Engineering, Faculty of Engineering and Natural Sciences, Sabanci University, 34956 Istanbul Turkey. He is now with the Department of Mechatronics Engineering, Faculty of Engineering and Design, Istanbul Commerce University, 34840 Istanbul Turkey. (e-mail: aftabak@ticaret.edu.tr).

S. Yesilyurt is with the Department of Mechatronics Engineering, Faculty of Engineering and Natural Sciences, Sabanci University, 34956 Istanbul Turkey. (e-mail: syesilyurt@sabanciuniv.edu).

systems as the means of propulsion and navigation solving key problems such as energy supply to artificial bio-inspired swimmers. In that regard, *E. Coli* species are considered as ideal examples of nano-scale devices [12].

A. Literature Review

Experimental work is carried out to manufacture rotary motors in micro-dimensions [13]; however, the size and complexity of the bacterial motor [14] are the bottlenecks in construction of a working replica, which compel researchers to execute artificial means of actuation [4], [8], [9] in order to achieve untethered bio-inspired micro-swimming.

In order to mimic natural swimmers, different actuation mechanisms are employed: generating planar waves driven by external magnetic fields on an artificial magnetic tail attached to a red blood cell [4], employing dedicated DC-motors to rotate helical tails in order to control the motion of the bio-inspired robot [8], or rotating the magnetic body of single-link helical swimmers with magnetic fields driven by Helmholtz coils in order to generate screw-like motion in viscous fluids [9], [10]. However, the energy efficiency of such artificial systems is actually lower than that of the bacterial motor [15].

As another strategy, some bacteria species are considered as the controllable means of actuation or propulsion for a variety of microsystems provided that given proper conditions and incentives they already possess the capability of maneuvering themselves [16]. One likely use for cybernetic microsystems is carrying out therapeutic operations in living tissue; by means of either controlling a single bacterium as a nano-robot or using the bacterium cell as an integral part in microfluidic microsystems for transport and actuation purposes [17], [18].

The possibility of moving objects via natural swimmers employing bacterial motor is experimentally studied with groups of *S. Marcescens* specimens attached to a cargo [19]. Authors investigated the propulsive forces, towing velocity and adherence durability in time. Martel [20] studied controlling the swimming direction of a magnetotactic bacteria (MTB) species, i.e. *M. Gryphiswaldense*, by inducing external magnetic fields, which in turn incorporates bacterial swimming with computer control. It is observed that the selected specimens follow the induced magnetic field lines. Martel *et al.* [21] manipulated single beads of 3 μm as cargo by controlling the velocity of individual MTBs. Authors further reported that reaching velocities faster than 100 $\mu\text{m/s}$ in magnitude is achievable [21]. Furthermore, building blocks, 80 μm in length, are piled over as in a two dimensional

pyramid by MTBs to demonstrate micro-assembly with bacteria [22].

Moreover, Uenoyama and Mitada [23] demonstrated that it is possible to neutralize a living natural micro-swimmer, e.g. *M. Mobile*, to eliminate toxic side effects; however, keep the cell wall and bacterial motor intact. Authors confirmed that, with a series of chemicals introduced in the environment, the bacterial motor can be reactivated. Experimental studies are reported on triggering and controlling the rotation rate of the flagella by introducing ions and chemicals to directly intervene the operation of the bacterial motor of certain species [24], [25]. An additional reported method of bacterial-manuevering is application of small electric currents to change the speed and direction of wave propagation [26]. The ability to control the swimming velocity and direction of natural micro/nano-swimmers indicates the need for reliable real-time analytical models.

Comprehensive mathematical models on the propulsion of microorganisms have been around for over sixty years. Hancock [27], using the slender body theory (SBT), formulated the resistive force theory (RFT) for particles undergoing quasi-static rigid-body motions in low Reynolds number viscous flows. In RFT method, fluid force vector acting on a moving object is linearly proportional to the rigid-body velocity vector relative to the stationary fluid. However, the RFT-model leads to omission of body-tail interactions: resistive force coefficients are based on local translations of slender tails [28], [29] and rigid-body motions of isolated bodies with well-known geometries [30], [31].

Keller and Rubinow [32] presented a total six degrees-of-freedom (dof) analytical model for natural micro-swimmers and pointed out that the local fluid resistance on a moving and deforming object of arbitrary shape is effected by the entire induced flow field. De la Torre and Bloomfield [33] modeled a representative micro-swimmer as a series of spherical bodies and studied the local effects of body-tail interactions on the rotating tail by hydrodynamic-interaction tensors. Authors concluded that the local hydrodynamic forces acting on the tail differ dramatically near the joint between body and tail due to the cross interactions. Johnson [34] discussed that the SBT method analysis of helical swimmers presents non-zero lateral forces based on the hydrodynamic interactions between swimmer's body and tail. Watari and Larson [35] discussed that the instantaneous flow field induced around a natural swimmer demonstrates transient behavior and the time-average of the flow field strength is smaller than its instantaneous magnitude. Authors also added that the hydrodynamic force on the swimmer's body is also influenced by induced flow fields. Above conclusions point out that the stationary fluid assumption is not accurate in the calculation of the drag force on the body.

Phan-Thien *et al.* [36] used the boundary-element-method (BEM) to solve Stokes equation and studied the effects of the geometry of helical tail and the geometry of a spheroid body on the forward velocity and hydrodynamic efficiency of the micro-swimmers. Authors discussed that the interaction between the two links decreases forward swimming velocity

and the hydrodynamic efficiency of the swimmer. Ramia *et al.* [37] carried out BEM analysis to obtain the motion of spheres with single rotating helical tail swimming in unbounded and bounded fluids. Authors studied the effect of hydrodynamic interaction on the overall propulsive and resistive behavior of the helical tail separately in detail. In both studies, the main focus was on the forces acting on the helical tail, swimming velocities, and hydrodynamic efficiency. It was concluded that the overall forward drag-resistance of the swimmer increases with hydrodynamic interactions.

Hydrodynamic models are of great importance because they are also used in determination of geometric properties and swimming trajectories for bacteria and spermatozoa species. RFT approach is employed to determine the high-order plane-wave form and to predict the motion of spermatozoa cells in full motion based on observations [38]. Planar wave actuation is more advantageous to investigate by a high-speed-and-resolution camera since the resultant motion is typically confined to the plane in which wave propagation takes place. However, tracking or observation of a bacterial cell in the third dimension proposes a more challenging task due the dimensions, thus observations on cells presented in the literature are mostly limited to constrained plane motions [39], [40], although there exists recent 3D-tracking examples for protists [41], [42]. Furthermore, three-dimensional trajectory construction studies are carried out with solutions of stochastic differential equations based on the observations on two-dimensional motion [43].

In addition to trajectory construction studies, resistive force theory is formerly employed in order to predict the propulsive forces generated by a number of artificial helical-swimmers in nm-, mm-, μm -, and cm-scale subject to various swimming conditions [44]-[49]. In a recent study, Mahoney *et al.* [47] utilized a RFT-based hydrodynamic model in order to predict necessary hydrodynamic forces in real-time and effectively control the velocity of a magnetically-actuated mm-length helical-swimmer with gravity compensation in an open-loop control scheme.

Furthermore, previous studies confirm that, as long as the inertial forces are significantly dominated by the viscous forces within the fluid, i.e. $\text{Re} < 0.1$, RFT approach is capable of predicting the time-averaged spatial velocities of an untethered swimmer, with an acceptable error, regardless of its actual size [48]-[50]. However, it is verified by Higdon [51] that power consumption of a micro-swimmer is miscalculated by the RFT method.

B. Main Contributions

Numerical studies conclude that the hydrodynamic interaction between body and helical tail is significant; but, a comprehensive analysis to quantify the drag force on the body in the presence of an actuated tail is not presented in literature to the best of our knowledge. Furthermore, the lateral oscillations of bacteria are not considered kinematically in analytical models so far. Given the complicated shape of the body-tail assembly and the hydrodynamic interactions

between them, conventional diagonal resistance matrix approach for isolated axisymmetric rigid particles in viscous flows is insufficient to account for the lateral oscillations of bacteria.

In this work, a CFD-model, which is validated with vertical in-channel swimming experiments on cm-scale bacteria-like robots, is employed to examine the 4-dof motion of a bio-mimetic swimmer comprised of a rotating rigid helical tail and a spherical body, which are held together with a revolute joint. Experiments are designed to eliminate all known physical phenomena, e.g. forces such as Brownian noise which is of importance in nano-scale [12], gravitational pull, and lubricated-friction, but far-field hydrodynamic interactions acting on the wet surfaces.

Initially, using the CFD-model, we studied swimming velocities with induced flow fields and obtained the hydrodynamic forces acting on the swimmer surface. Subsequently, we employed complex-impedance analysis in the RFT-model to introduce hydrodynamic interaction (HI) coefficients, which are embedded in the resistance matrix, to compensate for the flow field interactions and predict the instantaneous fluid resistance accurately for viscous swimming conditions regardless of the dimensions of bacteria or bacteria-like robots. It is verified that modified resistance matrix predicts time-dependent fluid forces with superior precision. Moreover, the effect of body and tail geometry is studied concluding that the hydrodynamic interaction is vastly dominated by the latter determining the swimming trajectory.

II. METHODOLOGY

A. RFT-model

RFT approach is well documented in [11], [27]-[29], and [32]: in the low Reynolds number, or creeping flow regime, the fluid resistance F_j , i.e. the drag force, acting on the moving particle along an arbitrary axis is linearly proportional to the velocity V_j of that particle. This is a valid approach to predict the drag force per unit length on a deformed slender body submerged in a highly viscous fluid with $Re < 0.1$ [28], [29]. Furthermore, the total fluid drag on a submerged particle freely moving in a viscous flow should add up to zero [52]. Using these two linear relationships, one can write down the equation of motion for a two-link helical swimmer as follows:

$$\mathcal{F}_b + \mathcal{F}_t = \mathbf{0}, \quad (1)$$

$$\mathcal{F}_{(b,t)} = -\mathbf{B}_{(b,t)} \mathbf{V}_{(b,t)} \quad (2)$$

where \mathbf{B} denotes the fluid resistance matrix for each link, namely body and tail denoted by the subscripts ‘ b ’ and ‘ t ’, respectively.

Tail resistance \mathbf{B}_t is obtained integrating the local force coefficients, which are projected onto the lab coordinates with the local frame rotations, over the actual chord length ℓ in the following fashion:

$$\mathbf{B}_t = \int_{\ell} \begin{bmatrix} \mathbf{R}\mathbf{C}\mathbf{R}^T & -\mathbf{R}\mathbf{C}\mathbf{R}^T\mathbf{S} \\ \mathbf{S}\mathbf{R}\mathbf{C}\mathbf{R}^T & -\mathbf{S}\mathbf{R}\mathbf{C}\mathbf{R}^T\mathbf{S} \end{bmatrix} d\ell \quad (3)$$

where \mathbf{R} is the rotation matrix between local Frenet-Serret frames and swimmer frame [53] (Fig. 1(a)), \mathbf{S} is the skew-symmetric matrix corresponding to the cross product with the time-dependent position vector \mathbf{P} , \mathbf{C} signifies the local fluid resistance matrix of the tail, and the superscript ‘ T ’ denotes the matrix transpose.

The position vector on a rotating left-handed helical tail with wavelength λ , angular rotation ω , and local amplitude $B(x)$ for an arbitrary \mathbf{x} -position can be specified by:

$$\mathbf{P} = [x \quad B(x)\cos(\omega t - kx) \quad B(x)\sin(\omega t - kx)]^T. \quad (4)$$

The local amplitude is given by $B(x) = B_o \min(1, \chi/0.1)$, where the position ramp function marks the converging end of the helical tail of length L with χ denoting the normalized \mathbf{x} -position along the tail. The maximum possible amplitude is indicated by B_o , and k in (4) signifies the wave number as $k = 2\pi/\lambda$. Rotational velocity of the tail is given by $d\mathbf{P}/dt = \mathbf{\Omega}_t \times \mathbf{P}$ with the actuation velocity of $\mathbf{\Omega}_t = [\omega \ 0 \ 0]^T$.

The local fluid resistance on the tail, denoted by \mathbf{C} in (3), is a diagonal matrix consisting of the resistance coefficients in the tangent, normal, and bi-normal directions. The coefficient set preferred in this text is [29]:

$$c_t = \frac{2\pi\mu}{\ln(0.18\lambda/\alpha r_t)}, \quad (5)$$

$$c_{(n,b)} = \frac{4\pi\mu}{\ln(0.18\lambda/\alpha r_t) + 0.5}, \quad (6)$$

where μ is the dynamic viscosity, r_t is the tail radius, and α is the ratio of tail length to chord length, i.e. $\alpha = L/\ell$.

The resistance matrix \mathbf{B}_b for the rigid body in (2) is:

$$\mathbf{B}_b = \begin{bmatrix} \mathbf{D} & \mathbf{G} \\ \mathbf{G}^T & \mathbf{E} \end{bmatrix}, \quad (7)$$

where \mathbf{D} and \mathbf{E} are 3×3 matrices indicating the translational and rotational resistances of the body, respectively. The off-diagonal \mathbf{G} matrix in (7) is zero if center of mass of the axisymmetric body lies along the long-axis of the swimmer. In this work, the resistance coefficients presented in [30] are used in analytical calculations. For an axisymmetric body, \mathbf{D} and \mathbf{E} are conventionally considered as diagonal matrices; for a spherical body, the diagonals of \mathbf{D} is equal to $3\pi\mu D_x$ and the diagonals of \mathbf{E} is equal to $\pi\mu D_x^3$ [30].

Rearranging the equation of motion, assuming that there are no other external stimuli on the system, one finds the velocity vector of the swimmer, which is denoted by the subscript ‘ s ’ in the left hand side, in the form:

$$\begin{bmatrix} \mathbf{V} \\ \boldsymbol{\Omega}_s \end{bmatrix} = -\mathbf{B}_s^T \mathbf{B}_t \begin{bmatrix} \mathbf{0} \\ \boldsymbol{\Omega}_t \end{bmatrix} \quad (8)$$

where \mathbf{B}_s is the effective fluid resistance matrix of the entire swimmer [48], [49]. Furthermore, one may impose ‘0’ on all elements of any row and column in \mathbf{B}_s^T to eliminate translational or rotational motion along a desired axis.

B. CFD-model

Fig. 1(b) demonstrates the micro-swimmer in the time-dependent fluidic domain $\Phi(t)$ bounded by the cylindrical channel. Consider a spherical body with a helical tail. One end of the helical tail is converging to its long axis, where the revolte joint is placed. This geometric design is a valid representation for some bacteria species [50]. Spherical body and helical tail are apart from each other with the tail radius in order to eliminate discontinuity in angular velocity boundary conditions. It is considered that both body and helical tail are neutrally buoyant with the surrounding medium, which is bounded by a cylindrical channel. Channel diameter is ten times that of the sphere diameter to eliminate the wall effects [54], and the swimmer is placed coaxially as Fig. 1(b) shows.

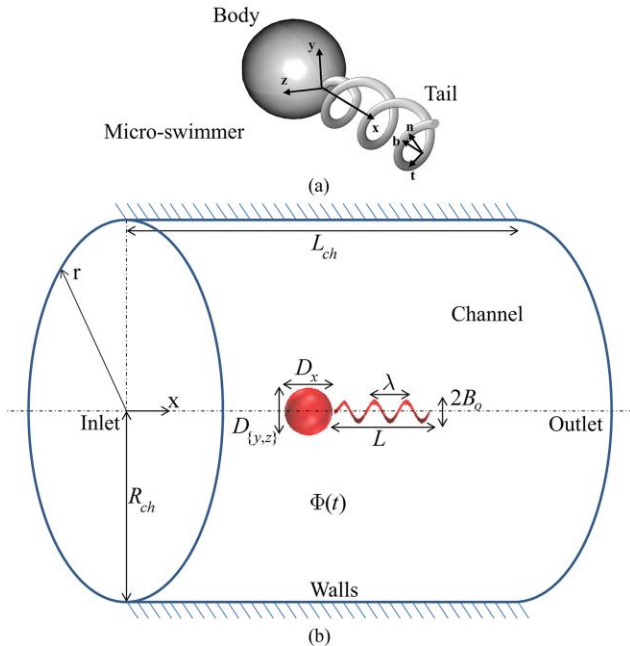


Fig. 1. Swimmer consisting of a spherical body and helical tail (top), submerged in a time-dependent viscous domain $\Phi(t)$, which is bounded by a coaxial cylindrical channel with a radius ten times that of the swimmer’s body (bottom).

Time-dependent incompressible Navier-Stokes equations govern the induced flow field in $\Phi(t)$ and are subject to continuity as follows:

$$\rho \left(\frac{\partial \mathbf{U}}{\partial t} + (\mathbf{U} - \dot{\mathbf{x}}_{\text{mesh}}) \cdot \nabla \mathbf{U} \right) = -\nabla p + \mu \nabla^2 \mathbf{U}, \quad (9)$$

$$\nabla \cdot \mathbf{U} = 0. \quad (10)$$

Here, \mathbf{U} and $\dot{\mathbf{x}}_{\text{mesh}}$ are respective fluid and mesh velocity vectors computed in $\Phi(t)$, ρ is the fluid density, and p denotes the hydrostatic pressure. Mesh of the swimmer is handled with arbitrary-Lagrangian-Eulerian (ALE) deformation in order to incorporate motion of swimmer boundaries with respect to stationary channel walls [55].

Zero-velocity and zero-pressure initial conditions are set for (9) and (10) initially, whereas no-slip boundary condition is imposed on stationary channel walls at all times. Normal stress vectors are set to zero at channel’s inlet and outlet to achieve open-flow boundary condition [56].

Position vector on the rotating left-handed helical tail is signified with a modified local amplitude function as $B(x) = B_0 \min(1, x/0.1) \min(1, f/4t)$, where f denotes the actuation frequency of the tail. The local amplitude increases with a time-ramp to ensure smooth transition of fully-developed rotating helical profile for the surrounding mesh.

Resultant body rotation rate vector, due to conservation of angular momentum, is given as $\boldsymbol{\Omega}_b = [\Omega_x \ 0 \ 0]^T$, and the corresponding fluid and mesh velocity boundary conditions on the surfaces of body, i.e. Ψ_b , and on the surfaces of tail, i.e. Ψ_t , are given respectively by:

$$\left. \begin{aligned} \mathbf{U} &= \mathbf{V} + \boldsymbol{\Omega}_b \times \mathbf{x}_s \\ \mathbf{u} &= \mathbf{V} \end{aligned} \right\} \Leftarrow \mathbf{x}_s \in \Psi_b, \quad (11)$$

$$\mathbf{U} = \mathbf{u} = \frac{d\mathbf{P}}{dt} + \mathbf{V} \Leftarrow \mathbf{x}_s \in \Psi_t, \quad (12)$$

where \mathbf{x}_s signifies the position vector of an arbitrary point on the surface of the swimmer with respect to its center of mass.

Resultant swimming velocity vectors are computed with force-free swimming constraints: in creeping flows, the fluid resistance on the entire surface of a self propelling swimmer adds up to zero [52]. Thus, the total instantaneous fluid force is set to zero in order to obtain rigid-body velocities satisfying zero-net-force and zero-net-torque constraints. The respective constraint equations for the hydrodynamic force and hydrodynamic torque acting on the entire surface of the swimmer are specified as follows:

$$\int_{\Psi_b + \Psi_t} [-p\mathbf{I} + \boldsymbol{\tau}] \mathbf{n} \, dA = \mathbf{0}, \quad (13)$$

$$\int_{\Psi_b + \Psi_t} \mathbf{x}_s \times [-p\mathbf{I} + \boldsymbol{\tau}] \mathbf{n} \, dA = \mathbf{0}. \quad (14)$$

Here, A denotes the surface area in contact with the viscous fluid, local surface normal vector is signified by \mathbf{n} , and $\boldsymbol{\tau}$ stands for the viscous stress tensor. Initial conditions are $\mathbf{V} = \mathbf{0}$ and $\boldsymbol{\Omega}_b = \mathbf{0}$; the constraint equations are solved at each time

increment based on the fluid resistance corresponding to the resultant rigid-body velocities of the preceding time-step combined with the tail rotation already in progress.

The last two rows of the constraints (13) and (14) are excluded in the CFD-model and the lateral rigid-body rotations, i.e. yaw and pitch, are eliminated. Omission of lateral rotations of the swimmer frame in the channel frame greatly simplifies the mesh deformation in $\Phi(t)$ eliminating numerical convergence issues and rotation matrix calculations between the two frames. Furthermore, Hyon *et al.* studied wiggling trajectories of bacteria and concluded that lateral rotations of the swimmer are observed clearly when the tail is not collinear with the symmetry axis. Otherwise, relatively straight trajectories are observed owing to much faster rate of rotation of the tail compared to the body [57].

C. Experiments

In this study a set of in-channel experiments, which are reported in detail elsewhere [49], are used to validate the CFD-model. A cm-scale bio-mimetic robot comprising of a cylindrical body and a rigid helical tail, which is actuated by a dedicated DC-motor, is used in experiments (Fig. 2(a)). One end of the rigid tail is deformed with a hyperbolic-tangent profile and attached to the rotor of the DC-motor, which constitutes the revolute joint allowing body and tail to rotate in opposite directions in order to mimic swimming of a bacterium with single helical tail [50].

Body of the bio-mimetic robot, which is a glass tube 18 mm in diameter (Fig. 2(b)), houses a DC-motor, a Li-Po battery pack, and a driver circuitry with IR-receiver to achieve remote control of motor actuation. A cylindrical cork is glued at the tip of the body to obtain neutral buoyancy and ensure stable swimming in the opposite direction to the gravitational pull without surface contact, and to restrict rigid-body rotations along the lateral directions by applying a restoring-torque (Fig. 2(c)). Properties of the bio-mimetic robot are listed in Table I.

Untethered bio-mimetic robot is placed inside constant-cross-section glass tube, 35 mm in diameter and 35 cm in length, filled with Si-oil of 3.5 Pa·s viscosity and 985 kg/m³ density. Both ends of the channel are sealed and the remote-controlled bio-mimetic robot swims vertically, opposite to the direction of gravitational attraction, along the centerline of the channel without touching its walls. A 30-fps CCD-camera is used to capture the swimming velocity, which is later resolved by visual inspection of the consecutive frames.

TABLE I
BIO-MIMETIC ROBOT AND EXPERIMENTAL SETUP

$2R_{ch}$	Channel Diameter	35 mm
L_{ch}	Channel Length	350 mm
$D_{[y,z]}$	Glass Body Diameter	18 mm
D_x	Total Body Length	50 mm
$2r_t$	Copper Wire Diameter	1 mm
-	Total Body Mass	11 g
-	Li-Po Pack Rating	70 mA·h with 3.7 V
ρ	Si-Oil Density	985 kg/m ³
μ	Si-Oil Viscosity	3.5 Pa·s
-	CCD-Camera Specs	640-by-480 Pixels @ 30 fps

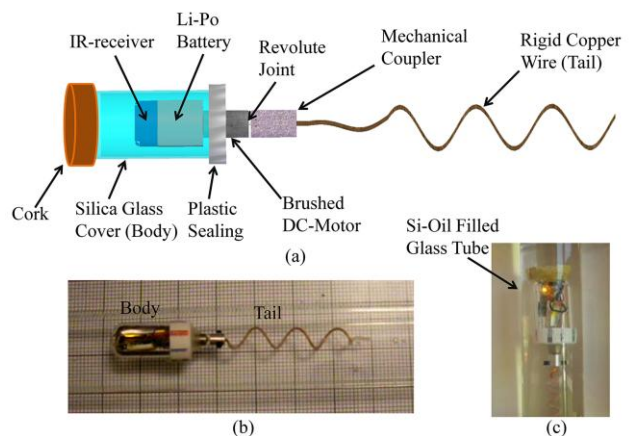


Fig. 2. Experimental setup: (a) bio-inspired robot consisting of a cylindrical body and helical tail; (b) robot inside a filled glass channel (no cork); (c) robot, with a cylindrical cork glued on the tip, swimming vertically.

III. RESULTS

A. RFT-model vs. Observations

The RFT-model is validated with the forward velocity and body rotation rate reported for certain bacteria species by Chattopadhyay and Wu [50]. Authors compared the effectiveness of SBT and RFT methods against the time-averaged forward velocities and body rotation rates observed in own experiments with *V. Alginolyticus*, *C. Crescentus*, and *E. Coli* minicell concluding that the former is more accurate in all cases [50]. It is noted that although some of the cell dimensions are close to or smaller than 1 μm , analytical approximation methods which only incorporates local flow fields or local resistance coefficients are still reliable.

Here, the RFT method is employed to ascertain the necessary corrections on the resistance coefficients of the axisymmetric bodies of the species, whose dimensions and wave properties are presented in Table II. Solutions are carried out by Adams-Bashforth-Moulton PECE solver [58] and average velocities are obtained over one complete period. Reported [50] and calculated velocity values and the determined correction factors to assure less than 0.1% error for RFT-model predictions are presented in Table III.

TABLE II
REPORTED GEOMETRIC PROPERTIES OF THE SELECTED SPECIES [50]

	f (Hz)	B_o (nm)	λ (μm)	L (μm)	r_t (nm)	D_x (μm)	$D_{[y,z]}$ (μm)
<i>V.</i>	571	140	1.2	3.7	16	4.6	0.7
<i>Alginolyticus</i>							
<i>C. Crescentus</i>	311	140	0.96	4.5	7	1.92	0.84
<i>E. Coli</i> minicell	78	190	2.3	6.2	12	0.82	0.82

For instance, the postulated corrected fluid resistance for spherical body of the *E. Coli* minicell along the x -axis are given as $3\pi\mu D_x \Upsilon_{T,x}$ for translation and $\pi\mu D_x^3 \Upsilon_{R,x}$ for rotation, respectively. Similar amplitude-correction factors for respective rigid-body translations and rotations, i.e. $\Upsilon_{T,x}$ and

$\Upsilon_{R,x}$, are embedded in (7) to predict the analytical fluid resistance for the species as provided in Table III.

Results point out that the resistance coefficients provided for an isolated axisymmetric blunt object are inadequate to predict the hydrodynamic forces and torques acting on its surface. The need for further study on the induced flow fields around helical micro/nano-swimmers in order to ascertain the cause of this discrepancy is clearly indicated.

TABLE III

VELOCITY COMPARISONS ON OBSERVATIONS [50] AND CALCULATIONS WITH REQUIRED CORRECTIONS (0.1% ERROR) FOR THE SELECTED SPECIES

	Observation		RFT Calculation		Corrections	
	U_x ($\mu\text{m/s}$)	Ω_x (Hz)	U_x ($\mu\text{m/s}$)	Ω_x (Hz)	$\Upsilon_{T,x}$	$\Upsilon_{R,x}$
V.	34	26	64	35	2.7	1.3
<i>Alginolyticus</i>						
<i>C.Crescentus</i>	30	31	42	33	1.9	1.06
<i>E.Coli</i>	14	31	16	31.006	1.4	1.002
minicell						

B. Validation of CFD-model with Experiments (Using Actual Dimensions)

Experimental studies are carried out on 4 different tails with different amplitude and wave length values. Each experiment is repeated a total of five times and forward velocity values are obtained from captured images. Error bars illustrated in Fig. 3 are obtained with 95% confidence interval. CFD simulations are carried out with actual dimensions and physical properties with $\Phi(t)$ being discretized with second order Lagrangian tetrahedral elements. Governing equations and force-free-swimming constraints are handled with PARDISO linear solver [59].

Fig. 3 demonstrates that the CFD-model predicts the effect of varying wave geometry on the forward swimming velocities reasonably well. Wave amplitude attains two distinct values, i.e. $B_o = \{4.5, 4.5, 7.5, 7.5\}$ mm, whereas each helical tail has a different wave length, i.e. $\lambda = \{12, 16, 11, 15\}$ mm with different apparent lengths $L_t = \{60, 93, 42, 56\}$ mm, respectively. Observed respective actuation frequencies for specified wave and tail geometries are $f = \{0.909, 0.937, 0.569, 0.569\}$ Hz, with an error interval of ± 0.01 Hz. The respective maximum and minimum errors are 13.6% and 8.8% in the forward velocity predictions, whereas 12.5% and 25% in body rotation rates. Forward swimming (Fig. 3(a)) and body rotation rate (Fig. 3(b)) results are presented in translational velocity ratio, i.e. $V_x/\lambda f$, and in rotational velocity ratio, i.e. Ω_x/ω , with respect to different wave numbers.

C. Validation of CFD-model with Observations on the E.Coli minicell (Using Dimensionless Analysis)

Dimensionless analysis, which is summoned in the following sections extensively, is a common practice in numerical investigations on micro/nano-swimmers [36], [37], [60], [61]. Furthermore, CFD-models benefit dimensionless-study approach with viscous flow regimes provided that suitable characteristic length- and time-scales are used [62].

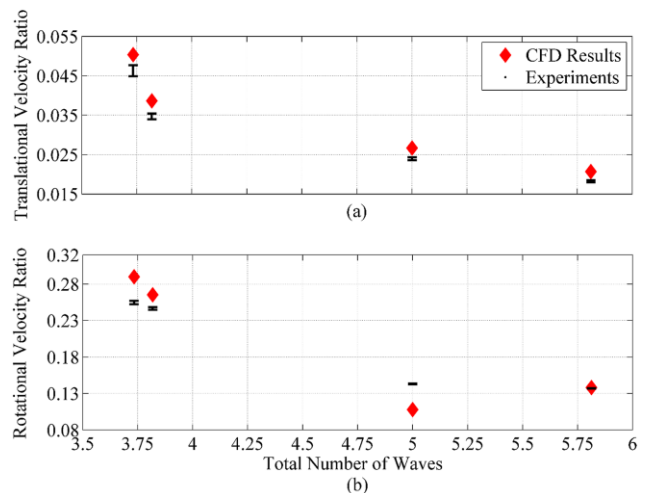


Fig. 3. Experiments (black lines) vs. CFD-model results (red diamonds): comparison on experiments and computations (a) with the ratio of forward velocity along the x-direction, V_x , to wave propagation velocity, $V_{wave} = f\lambda$; (b) with the ratio of body rotation rate, Ω_x , to tail rotation rate, ω .

Employing the computational model presented here, but with a channel diameter ten times that of the spherical body, we simulated nano-scale species *E. Coli* minicell [50] swimming fully-submerged in a large aquatic medium at room temperature in order to demonstrate that the accuracy does not deteriorate with the dimensionless analysis.

CFD-model is validated by means of observed geometric properties and calculated scaling constants (Table IV): spherical body diameter is the length-scale, f is the time-scale, and Reynolds number is $Re = \rho D_b^2 f / \mu$; therefore, dimensionless values used in the CFD-model are $D_{\{x,y,z\}} = 1$, $L = 7.56$, $r_t = 0.0146$, $B_o = 0.231$, $\lambda = 2.804$, $\rho = 1$, $f = 1$, and $\mu = 21376$, with velocity scaling factors $V_{scale} = 63.96 \mu\text{m/s}$ and $\Omega_{scale} = 78 \text{ Hz}$. CFD-model predicts $V_x = 0.194$ and $\Omega_x = 0.3647$. Thus, the equivalent dimensional velocities are $V_x = 12.408 \mu\text{m/s}$ and $\Omega_x = 28.453 \text{ Hz}$.

TABLE IV
GEOMETRIC AND PHYSICAL PROPERTIES, AND PREDICTED VELOCITIES WITH THE COMPUTATIONAL E. COLI MODEL

Symbol	Dimensional Value [50]	Dimensionless Value (CFD)
$D_{\{x,y,z\}}$	820 nm	1
r_t	12 nm	0.0146
L	6.2 μm	7.56
λ	2.3 μm	2.804
B_o	190 nm	0.231
f	78 Hz	1
ρ	1000 kg/m^3	1
Re	$4,678 \times 10^{-5}$	$4,678 \times 10^{-5}$
μ	$10^{-2} \text{ Pa}\cdot\text{s}$	21376
V_{scale}	63.96 $\mu\text{m/s}$	1
Ω_{scale}	78 Hz	1
V_x	14 $\mu\text{m/s}$	0.194
Ω_x	31 Hz	0.3647

Respective errors in the CFD-model prediction are 11.37% and 8.21% for forward velocity and body rotation rate compared to the observations [50]. Low error values with nano-scale body and tail radii, thus with the likely presence of

considerable Brownian noise [12], suggest that the model is sound. However, the CFD-model is primarily validated with the results of the cm-scale experiments because achieving individual control on the tail and wave parameters in nano-scale while keeping the body geometry fixed is unfeasible.

D. Swimmer Trajectory and Flow Fields Induced by The Tail Rotation

The governing equations (9) and (10) are cast in non-dimensional form in the following flow-field study; with the diameter of the body, D_b as the length scale and $2\pi/\omega$ as the time-scale, and hence $D_b\omega/2\pi$ as the velocity scale.

Therefore, the scaling Reynolds number is $Re = \rho D_b^2\omega/2\pi\mu$. Scaling Reynolds number used in the CFD-model is set to 10^{-2} to ensure creeping flow conditions. Complete list of variables used in the dimensionless base-case CFD simulation is presented in Table V.

Second order Lagrangian tetrahedral elements are used in CFD studies and the helical tail of the swimmer is discretized homogeneously resulting in 300.000 dof. Linear system of equations is solved with the PARDISO linear solver [59] and a second order backward difference formula with variable time-stepping for numerical integration with the maximum dimensionless time-step set to 0.025. Computations require approximately twenty hours on a high-end workstation to complete three full-periods of tail rotation.

The rigid-body velocity of the micro-swimmer in \mathbf{xyz} -frame is illustrated in Fig. 4. Forward velocity V_x (Fig. 4(a)) and body rotation rate Ω_x (Fig. 4(c)) reach to a steady value as the initial ramp is completed while the mesh is deformed to the extend where the local amplitude attains its maximum throughout the tail. Lateral velocities have out-of-phase sinusoidal behavior with zero time-average. Instantaneous lateral velocity is always comparable to the forward velocity and the $\pi/2$ phase between V_y and V_z (Fig. 4(b)) indicates helical trajectory in $\Phi(t)$.

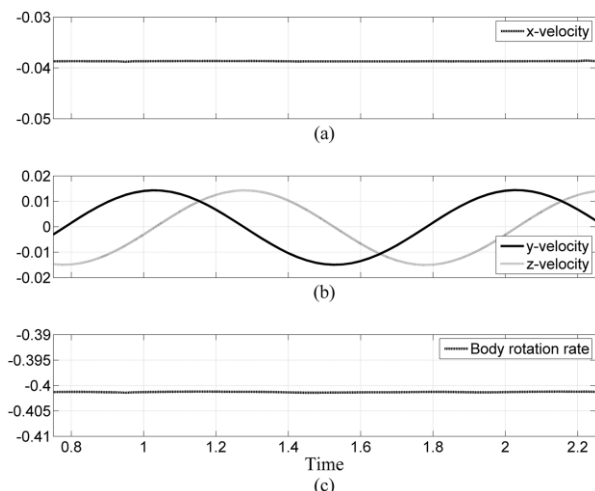


Fig. 4. Time-dependent velocity vector of the center of mass: (a) Forward velocity, i.e. along \mathbf{x} -axis; (b) lateral velocities; (c) body rotation rate, i.e. along \mathbf{x} -axis.

TABLE V
PARAMETERS FOR BASE-CASE CFD SIMULATION

Symbol	Parameter Name	Dimensionless Value
$D_{b,(x,y,z)}$	Spherical Body Diameter	1
r_t	Cylindrical Tail Radius	0.05
L	Cylindrical Tail Length	2
λ	Wave Length	$2/3$
B_o	Wave Amplitude	0.1
f	Propagation Frequency	1
ρ	Fluid Density	1
Re	Scaling Reynolds Number	10^{-2}
$\mu=1/Re$	Fluid Viscosity	100
L_{ch}	Cylindrical Channel Length	10
$2R_{ch}$	Cylindrical Channel Diameter	10

Studies on the induced flow field reveal that body and tail experience a mutual hydrodynamic interaction. A rotating but otherwise anchored helical tail submerged in viscous fluids would act as a pump [63]; but, if the anchoring force is released, the momentum exerted on the surrounding viscous domain is transformed into thrust partially. Given the fact that the wave propagation velocity is bigger than the propulsion velocity, rotating tail would propel itself while pushing the flow on the opposite direction. Thus the mechanical energy transferred into the surrounding fluid is dissipated simultaneously by the hydrodynamic drag due to resultant swimming action and by the forced-flow in the direction of wave propagation due to the pump-effect.

In order to single out the influence of tail rotation, translating and rotating bodies with non-rotating and rotating tails are studied, separately. First, a time-dependent velocity vector, which is identical to that obtained from the base-case CFD-model (Fig. 4), is imposed on the surface of a spherical body with a non-rotating helical tail attached on the right hand side as presented in Fig. 5(a). Boundary conditions on the non-rotating helical tail are set identically to that of the spherical body except for the rigid body rotation, thus the entire swimmer is being dragged through the unbounded viscous fluid. The streamlines depicting the flow field around the sphere become sparser signifying a decrease in viscous stresses especially at the back of the spherical body.

However, when the helical tail is allowed to rotate with an angular velocity of ω on its long axis, the streamline density behind the body increases considerably (Fig. 5(b)). This phenomenon is, in effect, a substantial increase in the velocity gradient due to normal stress build up at the back of the spherical body. The flow field driven by the pump-effect is also evident through the streamlines running down the \mathbf{x} -axis of the helical tail: streamlines behind the body are forced to follow the long axis of the rotating helix and purged at the back of the swimmer.

For sake of completeness and to demonstrate that the spatial compression of streamlines behind the body is a phenomenon regardless of its shape, we also investigated the induced flow field around a body with minimum drag, i.e. a geometry by design which was suggested by Bourot [64] to have less viscous resistance in contrast with a perfect sphere of same volume. Similar to the previous investigation, CFD

simulations are carried out for the streamlined body with a non-rotating tail (Fig. 6(a)) and with a rotating tail (Fig. 6(b)).

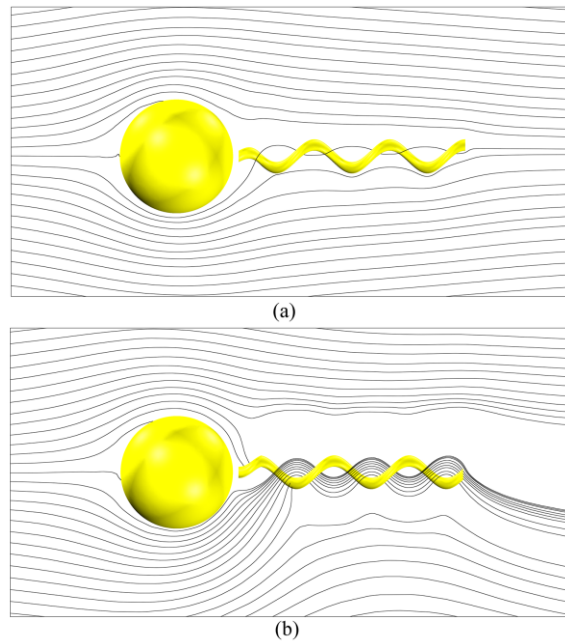


Fig. 5. Effect of tail rotation on the flow field depicted by thin black streamlines on xy -plane with the swimming velocities presented in Fig. 4 imposed as boundary conditions: (a) spherical body with non-rotating helical tail; (b) spherical body and helical tail, which rotate with Ω_x and ω , respectively. Streamline profiles are captured at $t = 1.275$ while instantaneous y -velocity of the swimmer is zero.

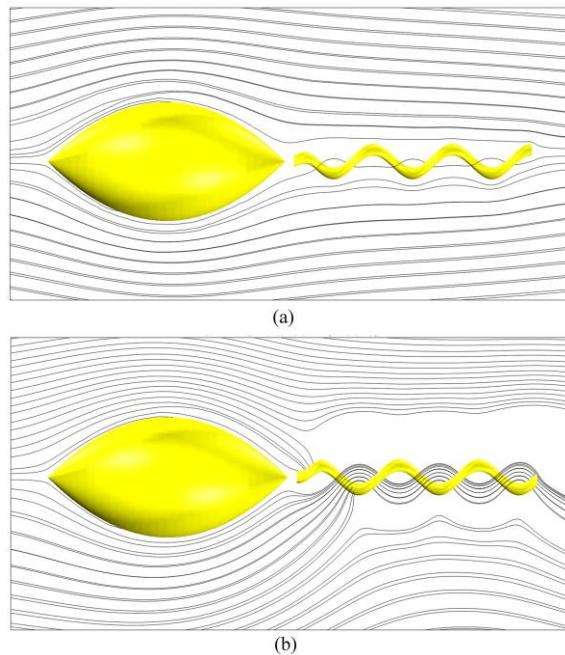


Fig. 6. Effect of tail rotation on the flow field around a body with streamlined-profile as suggested by Bourot [64] depicted by thin black streamlines on xy -plane: (a) streamlined-body with non-rotating helical tail; (b) streamlined-body and helical tail, which rotate with Ω_x and ω , respectively. Streamline profiles are captured at $t = 1.275$ while instantaneous y -velocity of the swimmer is zero.

In all cases, the short-axis of the studied body is equal to the radius of the perfect sphere, and the tail geometry remains unchanged. The boundary conditions are exactly the same as those imposed on the spherical body. The mesh quality, i.e. the maximum element size and element distribution, is also kept same as the preceding simulations.

The streamlines depicted in Fig. 6(a) follow the profile of the body and the separation does not occur until the revolute joint on the right hand side. Fig. 6(b) however, clearly demonstrates that the rotation of the tail disturbs the flow field around the body compressing the streamlines on the body near the tail on the right hand side. It is also noted that the streamline profiles are similar for the spherical body and the streamlined-body in the presence of rotating helical tail.

Based on the hydrodynamic interaction mediated by the induced flow field, it is concluded that the hydrodynamics of a swimmer's body is influenced by the rotation of its tail. In the next section, it is observed that the fluid resistance on the body greatly depends on the wave geometry. Additionally, the reader may find a detailed study on the effect of body shape in [65] where authors investigated the case of bacteria moving next to plane boundaries using BEM analysis, which is beyond the scope of this study, and concluded that the body shape is of importance for stable swimming trajectories.

E. Time-dependent Hydrodynamic Forces on Body, and The Hydrodynamic Interaction (HI) Coefficients

In this section, we incorporated cross-interactions due to the induced flow fields by respective correction coefficients in the fluid resistance matrix \mathbf{D} modified by casting the complex-impedance analysis in the form of amplitude-correction and phase-angle correction.

Necessary amplitude-corrections for the hydrodynamic interaction, i.e. Υ_T for rigid-body translation and Υ_R for rigid-body rotation, are calculated based on the ratio of hydrodynamic force obtained by CFD-model to the viscous sphere drag formulae presented in literature as follows for translation and rotation, respectively, as follows:

$$\Upsilon_{T,j} = \begin{cases} F_{j,avg} / D_{T,j} V_{j,avg} & \Leftarrow j = x \\ F_{j,max} / D_{T,j} V_{j,max} & \Leftarrow j = y, z \end{cases}, \quad (15)$$

$$\Upsilon_{R,j} = T_{j,avg} / D_{R,j} \Omega_{j,avg} \quad \Leftarrow j = x. \quad (16)$$

Here, $F_{j,\{avg,max\}}$ denotes the time-averaged and maximum normal force acting along an arbitrary axis, which is obtained by integrating total hydrodynamic stresses over the surface of the body in that direction. Similarly, $T_{j,avg}$ denotes the time-averaged viscous torque exerted on the surface of the swimmer's body along an arbitrary axis.

Time-dependent hydrodynamic force plots (Fig. 7) illustrate that a simple correction based on the force to velocity ratio given by (15) and (16) is inadequate to predict the instantaneous lateral hydrodynamic resistances acting on the body. Fig. 7 demonstrates that there exists a constant phase-shift between analytical lateral drag forces and the ones

obtained by the CFD-model: the phase-shift, in effect, is between swimming velocities and the hydrodynamic drag, in lateral directions.

The conventional diagonal drag-force coefficient matrix signifies a one-to-one relationship between elements of the velocity vector and respective fluid resistances for an isolated particle undergoing rigid-body translations without any cross-interactions. However, to account for the apparent phase-shift (Fig. 7), one may model the instantaneous lateral velocity and instantaneous lateral force vectors in complex planes, with respective amplitudes of V and F , as follows:

$$\begin{bmatrix} F_y \\ F_z \end{bmatrix} = \begin{bmatrix} F \exp(i\omega t) \exp(i\phi) \\ F \exp(i\omega t) \exp(i\phi) \exp(i\pi/2) \end{bmatrix}, \quad (17)$$

$$V_y + V_z = V \exp(i\omega t). \quad (18)$$

Thus, the elements of the conventional drag-force coefficient matrix in the RFT-model are modified in order to compensate for the HI-effects in the time-domain, and non-zero off-diagonal terms are introduced to account for the cross interactions, leading to an unsymmetrical and orthogonal matrix, as follows:

$$\mathbf{F}_b(\phi) = \begin{bmatrix} D_{T,x} \Upsilon_{T,x} & 0 & 0 \\ 0 & D_{T,y} \Upsilon_{T,y} \cos(\phi) & D_{T,y} \Upsilon_{T,y} \sin(\phi) \\ 0 & -D_{T,z} \Upsilon_{T,z} \sin(\phi) & D_{T,z} \Upsilon_{T,z} \cos(\phi) \end{bmatrix} \mathbf{V}, \quad (19)$$

where the phase-angle, ϕ , for the spherical body is obtained from Fig. 7 by solving the inverse problem for the phase-shift.

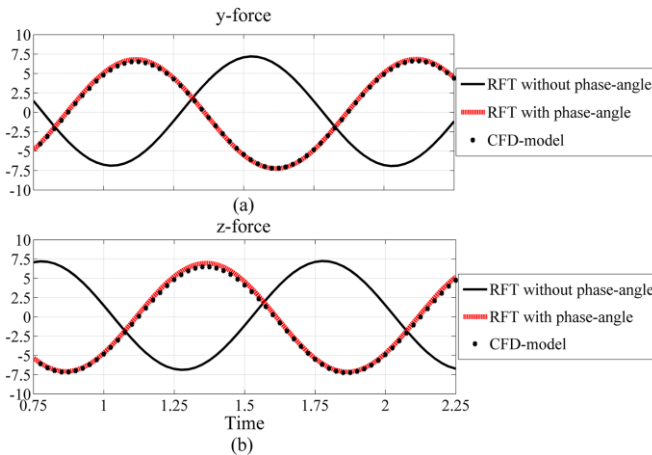


Fig. 7. Hydrodynamic force comparisons on analytical calculations and CFD-results: (a) y -drag exerted on body; (b) z -drag exerted on the body. Constant phase-shift between lateral velocities and lateral forces demand a modified resistance approach: conventional drag-force coefficient matrix is inapt to predict instantaneous viscous force exerted on the swimmer's body; however, the revised complex-impedance approach presented in (19) provides significantly improved results.

The forward rigid-body translation in (19) does not require phase-angle correction because the normal-force build-up at the back of the body is a steady effect due to continuous

rotation of the helical tail. Similarly, the hydrodynamic \mathbf{x} -torque acting on the body in (7) is also constant in time. The predicted HI-coefficients, amplitude-correction and the phase-angle, for the base-case CFD-model are presented in Table VI.

TABLE VI
PREDICTED HI-COEFFICIENTS AND PHASE-ANGLE FOR
THE BASE-CASE CFD-MODEL

Symbol	Parameter Name	Predicted Value
$\Upsilon_{T,x}$	HI-coefficient for \mathbf{x} -force	2.24
$\Upsilon_{T,\{y,z\}}$	HI-coefficient for lateral force	0.51
$\Upsilon_{R,x}$	HI-coefficient for \mathbf{x} -torque	1.09
ϕ	Phase-angle	1.17π

Parametric CFD simulations show that the effective forward fluid resistance $F_{x,avg}$ due to the forward velocity V_x varies linearly with total number of waves, i.e. N_λ , as depicted in Fig. 8(a). The lateral amplitude-correction, $\Upsilon_{T,\{y,z\}}$, reaches local maxima with $N_\lambda = \{0.25, 1.25, 2.25, 3.25, \dots\}$ and dips to local minima with $N_\lambda = \{1, 2, 3, \dots\}$ as given by Fig. 8(b). The main reason for this change in behavior is incomplete waves: with full waves, the $V_{\{y,z\}}$ components of the swimming velocity are small, thus the body does interact with the induced flow field minimally. On the other hand, incomplete waves induce lateral thrust and swimmer body moves sideways leading to further interaction with the surrounding flow field. A similar local minima and maxima relation is observed between $\Upsilon_{R,x}$ and N_λ : the variations are negligible and the overall relation can be practically deemed as linear; however, inversely proportional to varying N_λ as presented in Fig 8(c).

The relationship between $\Upsilon_{T,x}$ and wave amplitude is linear: the normal stress acting on the hemispherical surface on the right hand side of the body increases with increasing B_o , akin to increasing N_λ (Fig. 9(a)). The amplitude-correction of lateral HI-coefficient in lateral directions, $\Upsilon_{T,\{y,z\}}$, also varies linearly with wave amplitude; however, the amplification effect is significantly low (Fig. 9(b)). Lastly, $\Upsilon_{R,x}$ is inversely proportional to the wave amplitude, and varies slightly converging to 1 as B_o increases (Fig. 9(c)). Hence, the body is less affected by the tangential component of the flow field induced by the counter rotation of the tail.

The base-case CFD simulation computes a 1.17π phase-angle for the helical tail with $N_\lambda = 3$ and $B_o = 0.1$ as given in Table VI. Phase-angle dips to local minima for wave lengths shorter than half-wave on the tail, i.e. including quarter of a wavelength such as $N_\lambda = \{0.25, 1.25, 2.25, 3.25, \dots\}$ to be exact (Fig. 10(a)). Local minima of phase-angle coincide with the local maxima of amplitude-correction in lateral directions, as depicted by Fig. 8(b) and by Fig. 10(a). Moreover, the phase-angle reaches to local maxima with the presence of half waves, i.e. $N_\lambda = \{0.5, 1.5, 2.5, 3.5, \dots\}$.

Additionally, the phase-angle varies linearly with the wave amplitude B_o as presented in Fig. 10(b). The sensitivity of the phase-angle to the helical wave amplitude is evidently minute.

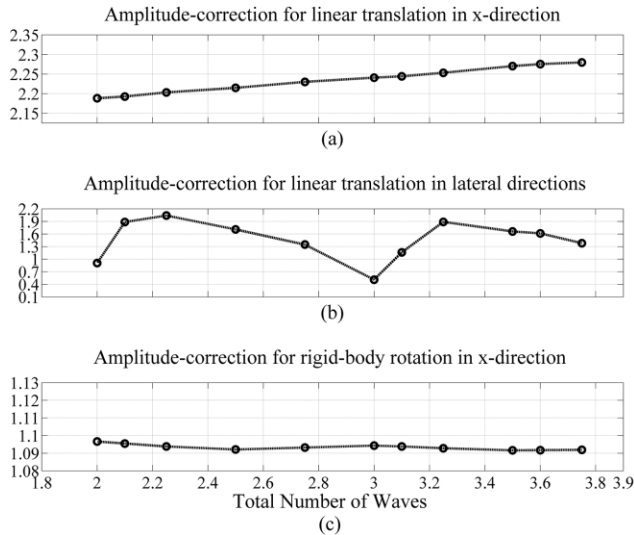


Fig. 8. Relation between the amplitude-correction of HI-coefficients and the helical wave geometry with respect to N_λ : (a) on the linear translation in x -direction with respect to N_λ ; (b) on the linear translation in lateral directions with respect to N_λ ; (c) on the x -rotation of the body with respect to N_λ .

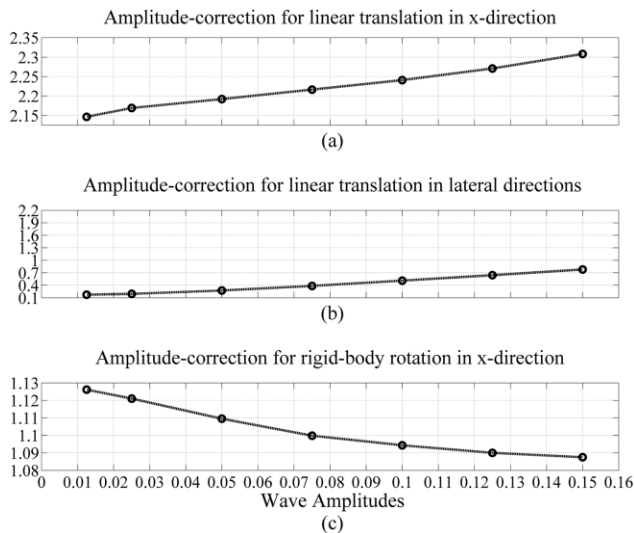


Fig. 9. Relation between the amplitude-correction of HI-coefficients and the helical wave geometry with respect to B_o : (a) on the linear translation in x -direction with respect to B_o ; (b) on the linear translation in lateral directions with respect to B_o ; (c) on the x -rotation of the body with respect to B_o .

IV. DISCUSSION

One can make use of an intensive molecular dynamics (MD) model to calculate hydrodynamic effects and deduce other forces in micro- and nano-scale experiments. Forces such as Brownian noise and other nano-scale interactions are also important, and must be studied by controlled experiments in micro- and nano-scales: once the hydrodynamic interaction effects are known, it will be easier to single out other physical phenomena shaping the swimming trajectory of a bacterium.

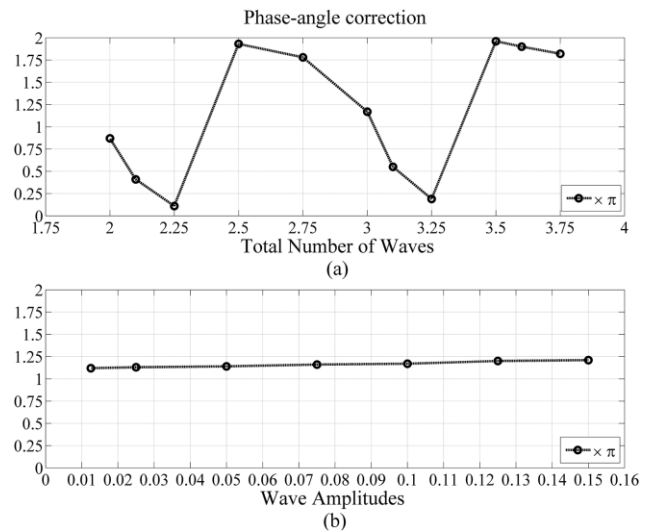


Fig. 10. Effect of wave geometry on phase-angle correction of HI-coefficients: (a) with respect to total number of waves on the helical tail, N_λ ; and (b) with respect to wave amplitude, B_o .

For instance, it is reported that, Brownian effect results in change of swimming direction of *E. Coli* cells in the long run [12]: the main trajectory is due to the hydrodynamic forces invoked by the wave propagation carried out on the tail; however, Brownian noise happens to introduce a stochastic course alteration approximately in every 10 seconds [12].

We conducted experiments with a cm-scale untethered bio-mimetic robot. Experiments are free of gravitational pull and contact forces. Furthermore, stochastic molecular interactions and electrostatic surface forces completely dilute due to the size of the robotic prototype. Thus, the hydrodynamic effects, which play a major role in the propulsion of micro/nano-swimmers as observed in nature and demonstrated by artificial mechanisms, are effectively isolated. Consequently, the viscous swimming experiment in this study are suitable as to be governed with a simple combination of rigid-body kinematics subject to force-free swimming constraints and Navier-Stokes equations subject to continuity. Moreover, replicating the experiment in smaller scales is unfeasible due to the impracticality of controlling the tail and wave parameters in micro- and nano-scales.

Without proper HI-corrections, body resistance is modeled with a diagonal matrix which calculates the time-averaged velocity vector computed by the CFD-model but erroneously: predicted forces and actual forces are out of phase in time-domain, thus constructed trajectory and predicted power consumption are incorrect. CFD simulations provide precious information on hydrodynamic interactions otherwise could not be easily singled out with mere experiments. HI phenomenon is explained with the flow field interactions between body and the tail, which are modeled with a complex-impedance analogy leading to HI-coefficients: with respective amplitude and phase-angle corrections, time-dependent force and velocity vectors are predicted with improved accuracy.

Experimental studies on observation and control of bacterial species will benefit from the improved resistance matrix approach: a bio-mimetic or cybernetic micro/nano-robot,

which is carrying out a predefined task, can be maneuvered successfully in real-time with construction of more accurate three-dimensional trajectories for control purposes during therapeutic operations, such as targeting cancerous tissue as recently discussed by Felfoul and Martel [18], or some properties of bacteria species which are hard to resolve by mere observation can be determined by the improved kinematic model with the help of time-dependent velocity information, as already demonstrated in the literature via observations on certain spermatozoa species [38].

For instance, the procedure to determine the HI-corrections from a conducted controlled experiment with MTBs, provided that all geometric properties are successfully observed, should be in this order: one first should search for the amplitude-correction factors satisfying the time-averaged forward velocities and the amplitude of lateral velocities. Then, one may find the phase-angle correction via solving the inverse problem for the phase-shift between observed and RFT-predicted lateral velocities. Moreover, HI-corrections will be useful even with relatively small wave amplitudes with respect to a large body or a bulky cargo being towed given that the B_s/D_b ratio in this study varies between 0.01 and 0.15. It is also noted that, for two-link helical swimmers, phase-angle and amplitude-corrections are not a function of one another.

V. CONCLUSIONS

Bio-mimetic micro/nano-robots and single-celled organisms are of great importance for future *in vivo* and *in vitro* applications in biomedicine such as minimal invasive surgery. Hence, improved hydrodynamic models based on well-known resistance coefficients will be extremely useful for accurate trajectory generation and control of natural micro/nano-swimmers. Hence, we focused on improving an otherwise well-known deterministic tool.

We conducted dimensionless time-dependent CFD simulations in order to study the flow fields induced by a helical swimmer in viscous domains. We qualitatively studied the effect of body geometry on the induced flow field: tail rotation amplifies the hydrodynamic stress increasing the spatial streamline density at the back of the spherical body. After examining the flow fields and swimmer trajectory in detail, we quantified the hydrodynamic interaction between the swimmer's body and rotating helical tail by introducing two hydrodynamic-interaction (HI) coefficients, i.e. amplitude and phase-angle corrections, based on complex-impedance analysis carried out on the time-dependent hydrodynamic force vector. The modified resistance matrix and the improved RFT-model are demonstrated to be indispensable in micro/nano-robotic applications with the ability to predict time-dependent force vectors accurately.

Furthermore, we quantitatively studied the relationship between HI-coefficients, and the wave geometry. It is demonstrated that the phase-angle of the lateral hydrodynamic-interaction has a nonlinear relationship with total number of waves and mildly sensitive to the wave amplitude: the nonlinear sensitivity to wave number indicates

the need for further study within a wider design space with higher resolution.

REFERENCES

- [1] S. Martel, O. Felfoul, J.-B. Mathieu, A. Chanu, S. Tamaz, M. Mohammadi, M. Mankiewicz, S. N. Tabatabaei, "MRI-based medical nanorobotic platform for the control of magnetic nanoparticles and flagellated bacteria for target interventions in human capillaries," *Int. J. Robot Res.*, vol. 28, no. 9, pp. 1169-1182, Sep. 2009.
- [2] B. J. Nelson, I. K. Kaliakatsos, J. J. Abbott, "Microrobots for minimally invasive medicine," *Annu. Rev. Biomed. Eng.*, vol. 12, pp. 55-85, Aug. 2010.
- [3] T. Honda, K. I. Arat, K. Ishiyama, "Micro swimming mechanisms propelled by external magnetic fields," *IEEE T. Magn.*, vol. 32, iss.5, pp. 5085-5087, Sep. 1996.
- [4] R. Dreyfus, J. Baudry, M. L. Roper, M. Fermigier, H. A. Stone, J. Bibette, "Microscopic artificial swimmers," *Nature*, vol. 437, pp. 862-865, Oct. 2005.
- [5] T. S. Yu, E. Lauga, A. E. Hosoi, "Experimental investigations of elastic tail propulsion at low Reynolds number," *Phys. Fluids*, vol. 18, iss. 9, 091701, Sep. 2006.
- [6] G. Kósa, M. Shoham, M. Zaaroor, "Propulsion method for swimming microrobots," *IEEE T. Robot.*, vol. 23, iss. 1, pp. 137-150, Feb. 2007.
- [7] L. Zhang, J. J. Abbott, L. Dong, B. E. Kratochvil, D. Bell, B. J. Nelson, "Artificial bacterial flagella: fabrication and magnetic control," *Appl. Phys. Lett.*, vol. 94, iss. 6, 064107, Feb. 2009.
- [8] B. Chen, S. Jiang, Y. Liu, Y. Yang, S. Chen, "Research on the kinematic properties of a sperm-like swimming micro robot," *J. Bionic Eng.*, vol. 7, suppl., pp. S123-S129, Sep. 2010.
- [9] L. Arcese, M. Fruchard, A. Ferreira, "Endovascular magnetically guided robots: navigation modeling and optimization," *IEEE T. Biomed. Eng.*, vol. 59, no. 4, pp. 977-987, Apr. 2012.
- [10] J. J. Abbott, K. E. Peyer, M. C. Lagomarsino, L. Zhang, L. Dong, I. K. Kaliakatsos, B. J. Nelson, "How should microrobots swim?," *The Int. J. Robot Res.*, vol. 28, iss. 11-12, pp. 1434-1447, Nov.-Dec. 2009.
- [11] C. Brennen, H. Winet, "Fluid mechanics of propulsion by cilia and flagella," *Annu. Rev. Fluid Mech.*, vol. 9, pp. 339-398, Jan. 1977.
- [12] H. C. Berg, "Navigation on a micron scale," in *Controlled Nanoscale Motion*, Lect. Notes Phys., vol. 711, H. Linke A. Månsson, Eds. Berlin: Springer-Verlag, 2007, pp. 1-13.
- [13] R. T. Tjeung, M. S. Hughes, L. Y. Yeo, J. R. Friend, "Surface acoustic wave micromotor with arbitrary axis rotational capability," *Appl. Phys. Lett.*, vol. 99, iss. 21, 214101, Nov. 2011.
- [14] H. C. Berg, "The rotary motor of bacterial flagella," *Annu. Rev. Biochem.*, vol. 72, pp. 19-54, Jul. 2003.
- [15] T. Fukuda, F. Arai, M. Nakajima, "Micro-nanorobotic manipulation systems and their applications," N.Y.: Springer-Verlag, 2013, pp. 137-139.
- [16] X. Xiong, M. E. Lidstrom, B. A. Parviz, "Microorganisms for mems," *J. Microelectromech. S.*, vol. 16, no. 2, pp. 429-444, Apr. 2007.
- [17] S. Martel, "Bacterial microsystems and microrobots," *Biomed. Microdevices*, vol. 14, iss. 6, pp. 1033-1045, Dec. 2012.
- [18] O. Felfoul, S. Martel, "Assessment of navigation control strategy for magnetotactic bacteria in microchannel: toward targeting solid tumors," *Biomed. Microdevices*, Jul. 2013. Available: <http://link.springer.com/content/pdf/10.1007/s10544-013-9794-4.pdf>
- [19] B. Behkam, M. Sitti, "Characterization of bacterial actuation of micro-objects," presented at The 2009 IEEE International Conference on Robotics and Automation, Kobe, Japan, May 12-17, 2009.
- [20] S. Martel, "Controlled bacterial micro-actuation," presented at The International Conference on Microtechnologies in Medicine and Biology, Okinawa, Japan, May 9-12, 2006.
- [21] S. Martel, C. C. Tremblay, S. Ngakeng, G. Langlois "Control manipulation and actuation of micro-objects with magnetotactic bacteria," *Appl. Phys. Lett.*, vol. 89, iss. 23, 233904, Dec. 2006.
- [22] S. Martel, M. Mohammadi, "A robotic micro-assembly process inspired by the construction of the ancient pyramids and relying on several thousand flagellated bacteria acting as micro-workers," presented at The 2009 IEEE/RSJ International Conference on Intelligent Robots and Systems, St. Louis, USA, Oct. 11-15, 2009.
- [23] A. Uenoyama, M. Miyata, "Gliding ghosts of mycoplasma mobile," *P. Natl. Acad. Sci. USA*, vol. 102, no. 36, pp. 12754-12758, Sep. 2005.

- [24] B. Behkam, M. Sitti, "Bacterial flagella-based propulsion and on/off motion control of microscale objects," *Appl. Phys. Lett.*, vol. 90, iss. 2, 023902, Jan. 2007.
- [25] K. Nogawa, M. Kojima, M. Nakajima, S. Kojima, M. Homma, T. Fukuda, "Rotational speed control of na⁻-driven flagellar motor by nano/micro dual pipettes," *IEEE T. Nanobiosci.*, vol. 8, iss. 4, pp. 341-348, Dec. 2009.
- [26] M. A. Sleight, "The biology of cilia and flagella," NY: The Macmillan Company, 1962, pp. 89-94.
- [27] G. J. Hancock, "The self-propulsion of microscopic organisms through liquids," *P. Roy. Soc. Lond. A Mat.*, vol. 217, no. 1128, pp. 96-121, Mar. 1953.
- [28] J. Gray, G. J. Hancock, "The propulsion of sea-urchin spermatozoa," *J. Exp. Biol.*, vol. 32, pp. 802-814, Dec. 1955.
- [29] J. Lighthill, "Flagellar hydrodynamics: the John von Neumann lecture," *SIAM Rev.*, vol. 18, no. 2, pp. 161-230, Apr. 1976.
- [30] H. C. Berg, "Random walks in biology," New Exp. Ed., N.J.: Princeton University Press, 1993, pp. 56-57&83-84.
- [31] F. Perrin, "Mouvement brownien d'un ellipsoïde (i). dispersion diélectrique pour des molécules ellipsoïdales," *J. Phys. Radium*, ser. 7, vol. 5, pp. 497-511, Oct. 1934.
- [32] J. B. Keller, S. I. Rubinow, "Swimming of flagellated microorganisms," *Biophys. J.*, vol. 16, iss. 2, pt. 1, pp. 151-170, Feb. 1976.
- [33] J. G. de la Torre, V. A. Bloomfield, "Hydrodynamic theory of swimming of flagellated microorganisms," *Biophys. J.*, vol. 20, iss. 1, pp. 49-67, Oct. 1977.
- [34] R. E. Johnson, "An improved slender-body theory for Stokes flow," *J. Fluid Mech.*, vol. 99, iss. 2, pp. 411-431, Jul. 1980.
- [35] N. Watari, R. G. Larson, "The hydrodynamics of a run-and-thumble bacterium propelled by polymorphic helical flagella," *Biophys. J.*, vol. 98, iss. 1, pp. 12-17, Jan. 2010.
- [36] N. Phan-Thien, T. Tran-Cong, M. Ramia, "A boundary-element analysis of flagellar propulsion," *J. Fluid Mech.*, vol. 184, pp. 533-549, Nov. 1987.
- [37] M. Ramia, D. L. Tullock, N. Phan-Thien, "Role of hydrodynamic interaction in the locomotion of microorganisms," *Biophys. J.*, vol. 65, iss. 2, pp. 755-778, Aug. 1993.
- [38] B. M. Friedrich, I. H. Riedel-Kruse, J. Howard, F. Jülicher, "High-precision tracking of sperm swimming fine structure provides strong test of resistive force theory," *J. Exp. Biol.*, vol. 213, pt. 8, pp. 1226-1234, Apr. 2010.
- [39] V. B. Shenoy, D. T. Tambe, A. Prasad, J. A. Theriot, "A kinematic description of the trajectories of *listeria monocytogenes* propelled by actin comet tails," *P. Natl. Acad. Sci. USA*, vol. 104, no. 20, pp. 8229-8234, May 2007.
- [40] Y. Pan, W. Lin, J. Li, W. Wu, L. Tian, C. Deng, Q. Liu, R. Zhu, M. Winklhofer, N. Petersen, "Reduced efficiency of magnetotaxis in magnetotactic coccoid bacteria in higher than geomagnetic fields," *Biophys. J.*, vol. 97, iss. 4, pp. 986-991, Aug. 2009.
- [41] T. Hasegawa, N. Ogawa, H. Oku, M. Ishikawa, "A new framework for microbotic control of motile cells based on high-speed tracking and focusing," presented at The 2008 IEEE International Conference on Robotics and Automation, Pasadena, CA, USA, May 19-23, 2008.
- [42] K. Drescher, K. C. Leptos, R. E. Goldstein, "How to track protists in three dimensions," *Rev. Sci. Instrum.*, vol. 80, iss. 1, 014301, Jan. 2009.
- [43] E. Gurarie, D. Grünbaum, M. T. Nishizaki, "Estimating 3d movements from 2d observations using a continuous model of helical swimming," *B. Math. Biol.*, vol. 73, iss. 6, pp. 1358-1377, Jun. 2011.
- [44] E. Lauga, W. R. DiLuzio, G. M. Whitesides, H. A. Stone, "Swimming in circles: motion on bacteria near solid boundaries," *Biophys. J.*, vol. 90, pp. 400-412, Jan. 2006.
- [45] A. Ghosh, P. Fischer, "Controlled propulsion of artificial magnetic nanostructured propellers," *Nano Lett.*, vol. 9, no. 6, pp. 2243-2245, May 2009.
- [46] L. Zhang, J. J. Abbott, L. Dong, K. E. Peyer, B. E. Kratochvil, H. Zhang, C. Bergeles, B. J. Nelson, "Characterizing the swimming properties of artificial bacterial flagella," *Nano Lett.*, vol. 9, no. 10, pp. 3663-3667, Sep. 2009.
- [47] A. W. Mahoney, J. C. Sarrazin, E. Bamberg, J. J. Abbott, "Velocity control with gravity compensation for magnetic helical microswimmers," *Adv. Robot.*, vol. 25, iss. 8, pp. 1007-1028, Jan. 2011.
- [48] A. F. Tabak, F. Z. Temel, S. Yesilyurt, "Comparison on experimental and numerical results for helical swimmers inside channels," presented at The 2011 IEEE/RSJ International Conference on Intelligent Robots and Systems, San Francisco, USA, Sep. 25-30, 2011.
- [49] A. F. Tabak, S. Yesilyurt, "In-channel experiments on vertical swimming with bacteria-like robots," to be presented at The 2013 IEEE/RSJ International Conference on Intelligent Robots and Systems, Tokyo, Japan, Nov. 3-7, 2013.
- [50] S. Chattopadhyay, X.-L. Wu, "The effect of long-range hydrodynamic interaction on the swimming of a single bacterium," *Biophys. J.*, vol. 96, iss. 5, pp. 2023-2028, Mar. 2009.
- [51] J. J. L. Higdon, "The hydrodynamics of flagellar propulsion: helical waves," *J. Fluid Mech.*, vol. 94, iss. 2, pp. 331-351, Sep. 1979.
- [52] G. I. Taylor, "Analysis of the swimming of microscopic organisms," *P. Roy. Soc. Lond. A Mat.*, vol. 209, no. 1099, pp. 447-461, Nov. 1951.
- [53] A. J. Hanson, H. Ma, "Quaternion frame approach to streamline visualization," *IEEE T. Vis. Comput. Gr.*, vol. 1, iss. 2, pp. 164-174, Jun. 1995.
- [54] R. G. M. van der Sman, "Effects of confinement on hydrodynamic interaction between a suspended sphere and stationary objects," *Comput. Fluids*, vol. 58, pp. 63-69, Apr. 2012.
- [55] F. Duarte, R. Gormaz, S. Natesan, S., "Arbitrary Lagrangian-Eulerian method for Navier-Stokes equations with moving boundaries," *Comput. Method. Appl. M. Eng.*, vol. 193, no. 45, pp. 4819-4836, Nov. 2004.
- [56] COMSOL AB, Comsol Multiphysics Modeling Guide, 2012.
- [57] Y. Hyon, Marcos, T. R. Powers, R. Stocker, H. C. Fu, "The wiggling trajectories of bacteria," *J. Fluid Mech.*, vol. 705, pp. 58-76, Aug. 2012.
- [58] L. F. Shampine, M. W. Reichelt, "The matlab ode suite," *SIAM J. Sci. Comput.*, vol. 18, iss. 1, pp. 1-22, Jan. 1997.
- [59] O. Schenk, K. Gärtner, "Solving unsymmetric sparse systems of linear equations with pardiso," *Future Gener. Comput. Sy.*, vol. 20, iss. 3, pp. 475-487, Apr. 2004.
- [60] F.-H. Qin, W.-X. Huang, H. J. Sung, "Simulation of small swimmer motions driven by tail/flagellum beating," *Comput. Fluids*, vol. 55, pp. 109-117, Feb. 2011.
- [61] R. Maniyeri, Y. K. Suh, S. Kang, M. J. Kim, "Numerical study on the propulsion of a bacterial flagellum in a viscous fluid using an immersed boundary method," *Comput. Fluids*, vol. 62, pp. 13-24, Jun. 2012.
- [62] A. F. Tabak, S. Yesilyurt, "Simulation-based analysis of flow due to traveling-plane-wave deformations on elastic thin-film actuators in micropumps," *Microfluid. Nanofluid.*, vol. 4, iss. 6, pp. 489-500, Jun. 2008.
- [63] O. Raz, J. E. Avron, "Swimming, pumping and gliding at low Reynolds numbers," *New J. Phys.*, vol. 9, pp. 437-445, Dec. 2007.
- [64] J.-M. Bourot, "On the numerical computation of the optimum profile in Stokes flow," *J. Fluid Mech.*, vol. 65, iss. 3, pp. 513-515, Sep. 1974.
- [65] H. Shum, E. A. Gaffney, D. J. Smith, "Modeling bacterial behavior close to a no-slip plane boundary: the influence of bacterial geometry," *P. Roy. Soc. Lond. A Mat.*, vol. 466, no. 2118, pp. 1725-1748, Jan. 2010.



Ahmet Fatih Tabak (M'09) received the Ph.D. degree in mechatronics engineering from Sabanci University, Istanbul, Turkey.

He is currently an Assistant Professor of mechatronics engineering with Istanbul Commerce University, Istanbul, Turkey. His research interests include fluid structure interactions, bio-inspired swimming micro-robots, bio-mechatronics, micro-fluidics, heat transfer, micro-pumps, and micro-systems.



Serhat Yesilyurt (SM'11) received the M.Sc. and Ph.D. degrees in Nuclear Engineering from the Massachusetts Institute of Technology, Cambridge, MA, USA.

He is currently an Associate Professor of mechatronics engineering with Sabanci University, Istanbul, Turkey. His research interests include bio-inspired swimming micro-robots, proton-exchange-membrane (PEM) fuel cells, micro-fluidics, heat transfer, simulation-based analysis and design, renewable and sustainable energy systems, and surrogate-based design optimization.